SCIENCE CHINA
Physics, Mechanics & Astronomy

• Article •

February 2020 Vol. 63 No. 2: 228711
https://doi.org/10.1007/s11433-019-1430-x

Chameleonlike metashells in microfluidics: A passive approach to adaptive responses

LiuJun Xu*, and JiPing Huang*

State Key Laboratory of Surface Physics, and Key Laboratory of Micro and Nano Photonic Structures (MOE), Department of Physics, Fudan University, Shanghai 200433, China

Received June 7, 2019; accepted August 20, 2019; published online October 22, 2019

Heat energy can transfer via convection, conduction, and radiation. Based on convection and conduction in microfluidics, people have designed and fabricated many novel devices. However, almost none of them has adaptivity, thus restricting practical applications under different conditions. To solve this problem, here we propose a passive approach to adaptive responses. That is, we consider the thermal convection-conduction process in microfluidic structures where Darcy's law and Fourier's law are both valid. By carefully designing two key parameters (i.e., tensorial thermal conductivity and tensorial permeability) of a metashell, we theoretically reveal that its effective properties (i.e., effective thermal conductivity and effective permeability) can adaptively change according to the inside object, thus yielding the "chameleonlike metashell". Further, this metashell is passive since it requires no prior knowledge of the inside object. We also report that the chameleonlike behavior can occur for anisotropic inside objects, nonuniform external fields, or even complex shapes. All theoretical analyses agree well with finite-element simulations. The chameleonlike metashell can act as an intelligent metamaterial in microfluidics for its adaptive responses, and it can also benefit other physical fields where convection plays a role, such as mass diffusion.

chameleonlike metashells, intelligent metamaterials, microfluidics

PACS number(s): 44.10.+i, 05.70.-a, 81.05.Zx

Citation: L. J. Xu, and J. P. Huang, Chameleonlike metashells in microfluidics: A passive approach to adaptive responses, Sci. China-Phys. Mech. Astron. **63**, 228711 (2020), https://doi.org/10.1007/s11433-019-1430-x

1 Introduction

Microfluidic structures have aroused wide research interest for their potential applications in chemistry, biology, optics, and information technology [1-8]. Recently, with the increasing focus on energy issues, researchers have turned their attention to heat management in microfluidic structures. The related mechanisms are mainly convection and conduction because radiation becomes insignificant in such cases.

Since the theory of transformation thermotics [9] was established in 2008, the ability of heat management has been largely improved. Many novel phenomena have been revealed with thermal metamaterials, such as thermal cloaks [9-17], thermal transparency [18-21], thermal bending [22-25], thermal camouflage/illusion [26-35], thermal Janus structures [36], thermal "golden touch" [37]. For fluid convection, a transformation theory was also established to control the fluid flow in porous media [38]. Recently, some work [39-41] considered the coupling between thermal conduction and fluid convection, even in transient regimes, thus yielding the concept of thermal cloak with fluid convection. These developments inspire us to explore more on metamaterials in microfluidic structures.

Although the existing achievements are exciting, a severe

*Corresponding authors (LiuJun Xu, email: 13307110076@fudan.edu.cn; JiPing Huang, email: jphuang@fudan.edu.cn)

problem is that these metamaterials exhibit almost no adaptivity, thus restricting applications under different conditions. With higher requirements of metamaterials, intelligence becomes one of the developing trends. Namely, metamaterials are expected to possess adaptivity to meet different requirements under different conditions, which can be called intelligent metamaterials.

To solve this problem, here we propose a passive approach which, however, can achieve adaptive responses. Concretely speaking, we design a metashell which can change its effective properties (i.e., effective thermal conductivity and effective permeability) adaptively according to different inside objects. Here, "passive" means that any prior knowledge of the inside object is not required; "metashell" indicates a manually-designed shell; and "inside object" can be regarded as a core surrounded by the metashell. This behavior is, to some extent, similar to chameleons whose colors can change adaptively according to different environments, and thus the metashell is also called "chameleonlike metashell" [42-44]. The potential application is to work as an all-purpose material. For example, materials are expected to be insulated to realize thermal protection, whereas they are expected to be conductive for heat dissipation. The chameleonlike metashell, due to its adaptive responses, may be an excellent candidate.

For thermal convection-conduction process in microfluidic structures (which are composed of porous media and incompressible fluid in this work), thermal conductivity and permeability are two key parameters. We carefully design the metashell and find a special condition to make its effective properties always equal to those of the inside object. Hence, adaptive responses are achieved. Then, we perform finite-element simulations to confirm the theoretical analyses. In what follows, let us start by presenting the theory.

2 Theory for chameleonlike metashells

In microfluidic structures, the passive thermal convection-conduction equation for steady states can be expressed as [40,41]:

$$\rho_{\mathrm{f}} C_{\mathrm{f}} (\boldsymbol{v} \cdot \nabla T) + \nabla \cdot \boldsymbol{j} = 0, \tag{1}$$

where ρ_{f} and C_{f} represent the density and heat capacity of the fluid, respectively. T denotes the equilibrium temperature of the porous media and the fluid at the contact point. The fluid velocity $\boldsymbol{v}$ and the conductive flux $\boldsymbol{j}$ are, respectively, given by Darcy's law and Fourier's law,

$$\boldsymbol{v} = -(\boldsymbol{\sigma}/\beta) \cdot \nabla P, \tag{2}$$

$$\boldsymbol{j} = -\boldsymbol{\kappa} \cdot \nabla T, \tag{3}$$

where $\boldsymbol{\sigma}$ is the tensorial permeability of the porous media, and β is the dynamic viscosity of the fluid. P denotes pressure. $\boldsymbol{\kappa}$ is the average tensorial thermal conductivity of the porous media plus the fluid which is given by $\boldsymbol{\kappa} = (1-\phi)\boldsymbol{\kappa}_{\mathrm{s}} + \phi\kappa_{\mathrm{f}}$, where $\boldsymbol{\kappa}_{\mathrm{s}}$ and ϕ are, respectively, the tensorial thermal conductivity and the porosity of the porous media, and κ_{f} is the thermal conductivity of the fluid. For a passive process, the fluid velocity $\boldsymbol{v}$ is always divergence-free [40,41], and we suppose that the conductive flux $\boldsymbol{j}$ is also divergence-free for the convenience of discussion,

$$\nabla \cdot \boldsymbol{v} = 0, \tag{4}$$

$$\nabla \cdot \boldsymbol{j} = 0. \tag{5}$$

Further, since there is only one type of fluid in our cases, β becomes a constant which can be ignored in eq. (4). Then, eqs. (4) and (5) can be unified as:

$$\nabla \cdot (-\boldsymbol{\omega} \nabla \Omega) = 0, \tag{6}$$

where $\boldsymbol{\omega} = \boldsymbol{\sigma}$ or $\boldsymbol{\kappa}$, and $\Omega = P$ or T. In what follows, the discussion of $\boldsymbol{\sigma}$ and $\boldsymbol{\kappa}$ will be unified to that of $\boldsymbol{\omega}$ because they follow the same dominant equation (eq. (6)).

Now, we consider the system as described in Figure 1(a). The scalar parameters of region I (ω_1) and region III (ω_3) are the same ($\omega_1 = \omega_3$), and the tensorial parameter of region II

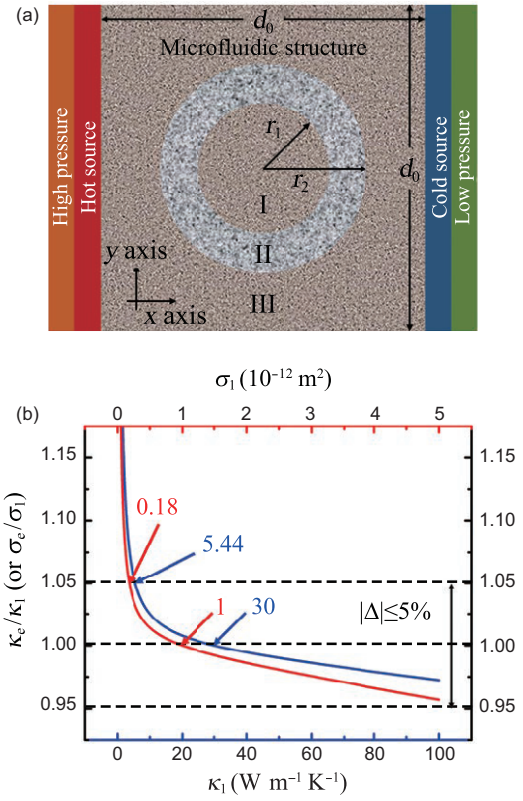

Figure 1 (Color online) Concept of the chameleonlike metashell. (a) A schematic diagram of the research system; (b) the theoretical performance of the chameleonlike metashell.

(the chameleonlike metashell, $\boldsymbol{\omega} = \mathrm{diag}(\omega_{rr}, \omega_{\theta\theta})$) is written in cylindrical coordinates. The effective scalar parameter of region I plus region II (denoted by ω_e) can be calculated by [37]

$$\omega_e = c\omega_{rr}\frac{\omega_1 + c\omega_{rr} + (\omega_1 - c\omega_{rr})\, f^c}{\omega_1 + c\omega_{rr} - (\omega_1 - c\omega_{rr})\, f^c}, \tag{7}$$

where $f = (r_1/r_2)^2$ is the core fraction, and $c = \sqrt{\omega_{\theta\theta}/\omega_{rr}}$ represents the anisotropy degree. Eq. (7) is a standard result for calculating the effective thermal conductivity [37]. Since permeability follows the exactly same dominant equation as thermal conductivity, eq. (7) can also explain the effective permeability.

The chameleonlike metashell features the same property as the inside object, which can be mathematically defined as:

$$\omega = \omega_1, \tag{8}$$

where ω is the effective scalar parameter with respect to the tensorial one ($\boldsymbol{\omega}$). Since the effective scalar parameters of region I and region II are both ω_1, the effective parameter of region I plus region II has the only possibility to be

$$\omega_e = \omega_1. \tag{9}$$

Throughout the process, we do not restrict the value of ω_1, and hence the ideal chameleonlike metashell is characterized by $\omega_e/\omega_1 = 1$.

In all cases, the exact realization of eq. (9) is impossible. In spite of this difficulty, we find a special condition for the metashell to make eq. (9) approximately valid, say,

$$\omega_{\theta\theta} \ll \omega_1 \ll \omega_{rr}. \tag{10}$$

Then, we discuss the role of eq. (10). First, it gives $\omega_{\theta\theta}/\omega_{rr} \to 0$, indicating $c \to 0$ and $f^c \approx 1 + c\ln f$, and thus eq. (7) can be reduced to

$$\begin{aligned}\omega_e &\approx c\omega_{rr}\frac{\omega_1 + c\omega_{rr} + (\omega_1 - c\omega_{rr})(1 + c\ln f)}{\omega_1 + c\omega_{rr} - (\omega_1 - c\omega_{rr})(1 + c\ln f)} \\ &= \omega_{rr}\frac{2\omega_1 - \omega_{\theta\theta}\ln f}{2\omega_{rr} - \omega_1 \ln f}.\end{aligned} \tag{11}$$

Second, it indicates that $\omega_{\theta\theta}$ (or ω_1) can be regarded as a small quantity with respect to ω_1 (or ω_{rr}), and thus eq. (11) can be further simplified as:

$$\omega_e \approx \omega_1. \tag{12}$$

In the whole process, we just suppose a variation range for ω_1 given by eq. (10), rather than a concrete value. Therefore, eq. (12) can be also expressed as $\omega_e/\omega_1 \approx 1$, which is the result that we expect to achieve.

So far, the mechanism of the chameleonlike metashell has been theoretically uncovered (eq. (10)). It is an approximate result, so we need to use practical parameters to check the performance of the chameleonlike metashell. We set the tensorial thermal conductivity and the tensorial permeability of the chameleonlike metashell to be $\boldsymbol{\kappa} = \mathrm{diag}(1500, 0.6)\,\mathrm{W\,m^{-1}\,K^{-1}}$ and $\boldsymbol{\sigma} = \mathrm{diag}(50, 0.02) \times 10^{-12}\,\mathrm{m^2}$, respectively. The two parameters are both characterized by a large radial component and a small tangential component as required by eq. (10). Throughout this work, $\boldsymbol{\kappa}$ (or κ) is always the average tensorial (or scalar) thermal conductivity of the porous media plus the fluid. Therefore, the thermal conductivity of the porous media $\boldsymbol{\kappa}_\mathrm{s}$ is given by $\boldsymbol{\kappa}_\mathrm{s} = (\boldsymbol{\kappa} - \phi\kappa_\mathrm{f})/(1-\phi)$. Then, we plot the ω_e/ω_1 curve changing with ω_1 according to eq. (7); see Figure 1(b). We find that the relative error $\Delta = (\omega_e - \omega_1)/\omega_1$ is below 5% when κ_1 ranging from 5.44 to $100\,\mathrm{W\,m^{-1}\,K^{-1}}$, and σ_1 ranging from 1.8×10^{-13} to $5 \times 10^{-12}\,\mathrm{m^2}$. The results indicate that the chameleonlike metashell can work in a wide range. Despite of the good performance, the requirement is that ω_{rr} should be about four orders of magnitude bigger than $\omega_{\theta\theta}$.

3 Simulations for chameleonlike metashells

To validate the theoretical analyses, we further perform finite-element simulations for steady states based on the commercial software COMSOL MULTIPHYSICS (http://www.comsol.com/); see Figures 2-5. In all simulations, the parameters of the chameleonlike metashell and the normal shell are kept unchanged; say, $\boldsymbol{\kappa} = \mathrm{diag}(1500, 0.6)\,\mathrm{W\,m^{-1}\,K^{-1}}$, $\boldsymbol{\sigma} = \mathrm{diag}(50, 0.02) \times 10^{-12}\,\mathrm{m^2}$ for the chameleonlike metashell, and $\kappa = 30\,\mathrm{W\,m^{-1}\,K^{-1}}$, $\sigma = 10^{-12}\,\mathrm{m^2}$ for the normal shell. The parameters of regions I and III are kept the same except for additional statement. For case 1: $\kappa = 6\,\mathrm{W\,m^{-1}\,K^{-1}}$ and $\sigma = 5 \times 10^{-12}\,\mathrm{m^2}$; for case 2: $\boldsymbol{\kappa} = [(30, -15), (-15, 30)]\,\mathrm{W\,m^{-1}\,K^{-1}}$ and $\boldsymbol{\sigma} = [(1, 0.5), (0.5, 1)] \times 10^{-12}\,\mathrm{m^2}$ (which are written in Cartesian coordinates); and for case 3: $\kappa = 60\,\mathrm{W\,m^{-1}\,K^{-1}}$ and $\sigma = 5 \times 10^{-13}\,\mathrm{m^2}$, which are all in the range of 5% relative error as shown in Figure 1(b). The porosity of the porous media in regions I, II, and III is $\phi = 0.8$. The fluid in regions I, II, and III is water whose parameters are $\rho_\mathrm{f} = 10^3\,\mathrm{kg\,m^{-3}}$, $C_\mathrm{f} = 4.2{\times}10^3\,\mathrm{J\,kg^{-1}\,K^{-1}}$, $\beta = 10^{-3}\,\mathrm{Pa\,s}$, and $\kappa_\mathrm{f} = 0.6\,\mathrm{W\,m^{-1}\,K^{-1}}$. The size parameters are $r_1 = 2{\times}10^{-5}\,\mathrm{m}$, $r_2 = 3.2 \times 10^{-5}\,\mathrm{m}$, and $d_0 = 10^{-4}\,\mathrm{m}$. The temperature difference and the pressure difference are set to $\Delta T = 40\,\mathrm{K}$ and $\Delta P = 200\,\mathrm{Pa}$ except for Figure 5. Although eq. (7) itself does not restrict the size of the chameleonlike metashell, certain restrictions should be satisfied to ensure the validity of Darcy's law. Namely, the designed parameters lead to the

Reynolds number $Re = vr_2\rho_f/\beta \ll 10$ (linear laminar flow region) and $\sigma \ll r_2^2$, which make Darcy's law valid.

Then, we explain the finite-element simulations in Figures 2-5 in detail. The complete information of the thermal convection-conductive process can be reflected by the scalar fields; say, the temperature distributions and the pressure distributions. Therefore, we plot both temperature distributions and pressure distributions in what follows.

Figure 2 demonstrates the adaptive responses of the chameleonlike metashell from an isotropic case to an anisotropic case. When the chameleonlike metashell is placed in case 1 (Figure 2(a) and (b)), it can adaptively change its effective properties (i.e., effective thermal conductivity and effective permeability) to adapt to the inside object. As a result, the scalar fields outside the metashell is the same as those outside the comparative shell; see Figure 2(i) and (j). However, the normal shell fails to change adaptively which results in the different scalar fields outside the shells; see Figure 2(e) and (f). Then, we put the chameleonlike metashell in case 2 with anisotropic parameters; see Figure 2(c) and (d). Again, the chameleonlike metashell changes with the inside anisotropic object, and exhibits the same scalar fields as those outside the comparative shell; see Figure 2(k) and (l). By contrast, the normal shell still fails to change adaptively; see Figure 2(g) and (h). Here, the divergence of the conductive flux is not zero, but eq. (7) still works and yields the chameleonlike behavior. This results from that divergency-free (eq. (5)) is not a requirement because the effective thermal conductivity (eq. (7)) is independent of the divergency of the conductive flux.

The finite-element simulations in Figure 2 are performed with uniform external fields along x axis. Then, we change only the direction of the pressure field along y axis, and put the chameleonlike metashell in case 1; see Figure 3(a) and (b). We also set a hot source in the top-left corner and a high pressure in the bottom-right corner to generate nonuniform fields, and put the chameleonlike metashell in case 3; see Figure 3(c) and (d). The same scalar fields outside the shells between Figure 3(a), (b), (i), and (j) (or Figure 3(c), (d), (k), and (l)) indicate that the chameleonlike metashell does work for different external fields. However, the normal shell fails; see Figure 3(e), (f), (g), and (h). For clarity of Figure 3(g) and (h), we can compare the contour lines near the shells; say, the first and forth contour lines from the right-bottom corner of Figure 3(g) and (k), and the first and forth contour lines from the left-top corner of Figure 3(h) and (l). The chameleonlike behavior still occurs for nonuniform external fields because eq. (7) is valid without the requirement of external fields.

Further, we check whether the shape of the chameleonlike metashell will affect the adaptive behavior. We change the shape of the chameleonlike metashell into a square, and put it in case 1; see Figure 4(a) and (b). We also design a more complex shape, and put it in case 3; see Figure 4(c) and (d). By comparing the scalar fields outside the shells between Figure 4(a), (b), (i), and (j) (or Figure 4(c), (d), (k), and (l)), we find that the adaptive behavior still exists for different shapes. Meanwhile, the normal shell fails; see Figure 4(e), (f), (g), and (h). For clarity of Figure 4(g) and (h), we can compare the second and penultimate contour lines from the left side between Figure 4(g) and (k) (or Figure 4(h) and (l)).

Finally, we consider two cases with temperature difference $\Delta T = 20\,\mathrm{K}$ and pressure difference $\Delta P = 400\,\mathrm{Pa}$; see Figure 5. The other parameters of the left two columns in

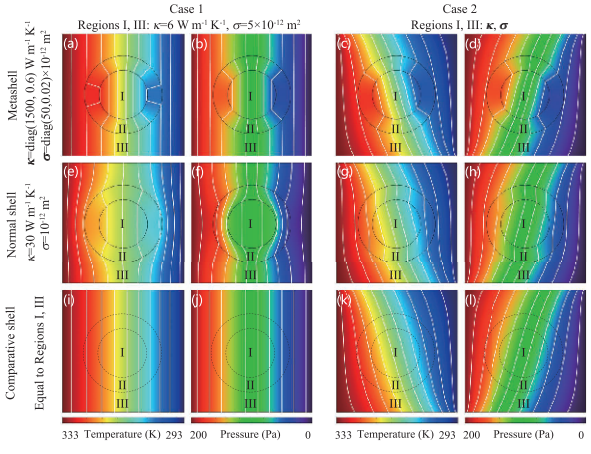

Figure 2 (Color online) Finite-element simulations for the chameleonlike metashell. White lines represent contour lines. Different cases only represent different parameters of regions I and III. Chameleonlike metashell, normal shell, and comparative shell are placed in the first, second, and third rows, respectively. The external fields are uniform along x axis. Case 1 is isotropic, whereas case 2 is anisotropic. The comparative shell in the third row is represented by dashed lines because it is essentially the same as regions I and III.

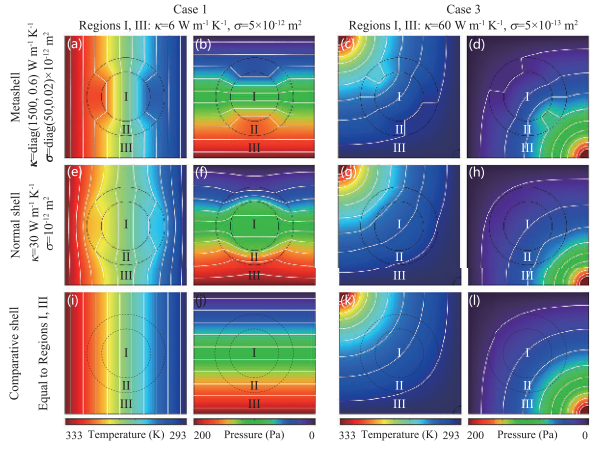

Figure 3 (Color online) Finite-element simulations with different external fields. The pressure field in the second column is along y axis. The temperature field in the third column is nonuniform, and the cold source is set at the bottom and right boundaries. The pressure field in the forth column is also nonuniform, and the low pressure is set at the top and left boundaries. Other boundaries are set with insulation and no flow conditions.

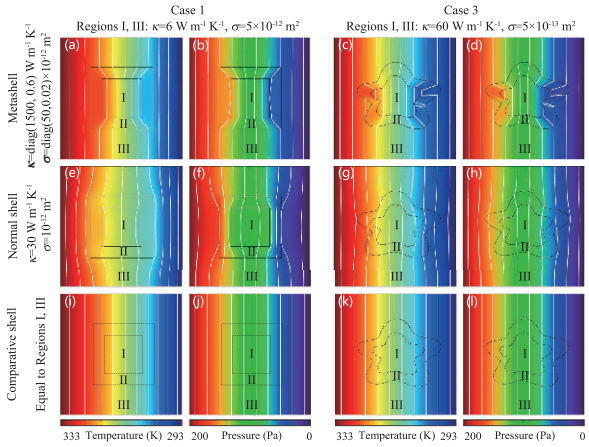

Figure 4 (Color online) Finite-element simulations with different shapes. The widths of the inner and outer square in the left two columns are 3.2×10^{-5} and 5.12×10^{-5} m, respectively. The inner parametric line in the right two columns is $x = 2 \times 10^{-6}\,[10 + \cos\theta - \cos(2\theta) + 2\sin(5\theta)]\cos\theta$, $y = (10/7) \times 10^{-6}\,[10 + \cos\theta - \cos(2\theta) + 2\sin(5\theta)]\sin\theta$, $\theta \in [0, 2\pi)$. The outer one is 1.6 times as big as the inner one.

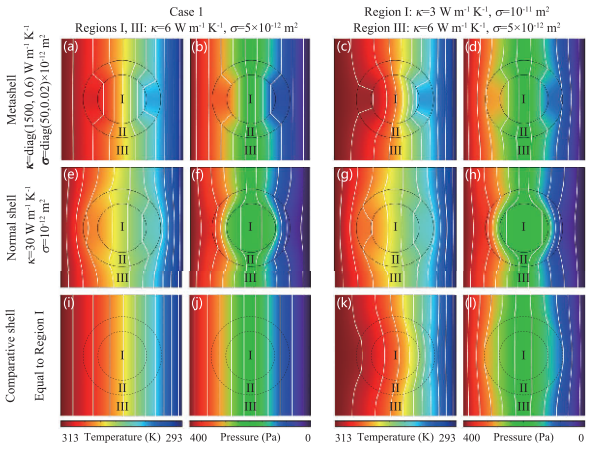

Figure 5 (Color online) Finite-element simulations with different temperature and pressure differences. The parameters of regions I and III in the left two columns are the same; say case 1. The parameters of regions I and III in the right two columns are different, and the parameters of the comparative shell is set to be the same as those of region I.

Figure 5 are the same as those for case 1 in Figure 2. Certainly, the chameleonlike behavior still occurs because eq. (7) is valid without the requirement of external fields; see the left two columns of Figure 5. Moreover, it is just for convenience to set the parameters of region III to be the same as those of region I. In fact, whatever the parameters of region III are, the chameleonlike metashell can always imitate the properties of the inside object. Thus, we set the parameters of regions I and III to be different in the right two columns in Figure 5; say $\kappa = 3\,\mathrm{W\,m^{-1}\,K^{-1}}$ and $\sigma = 10^{-11}\,\mathrm{m^2}$ for region I, and $\kappa = 6\,\mathrm{W\,m^{-1}\,K^{-1}}$ and $\sigma = 5 \times 10^{-12}\,\mathrm{m^2}$ for region III. The same temperature and pressure profiles outside the metashell and the comparative shell indicate that the chameleonlike metashell can always imitate the properties of the inside object; see Figure 5(c), (d), (k), and (l). However, the normal shell always fails; see Figure 5(g) and (h).

So far, we have shown the robustness of the chameleonlike metashell under more complicated conditions; say, for anisotropic cores, nonuniform external fields, and complex shapes. These results help to conclude that as required by eq. (10), eq. (12) still holds regardless of such complicated conditions.

4 Discussion and conclusion

For the experimental realization of the chameleonlike metashell, the key is to realize a large radial component and a small tangential component of the tensorial thermal conductivity (or the tensorial permeability) as required by eq. (10). A reliable method is to design a fan-shaped layer structure [45, 46] with two distinct materials whose thermal conductivities (or permeabilities) should differ up to four orders of magnitude. We design the layer structures with two isotropic materials presented in Figure 6(a)-(c), whose effective radial and tangential properties are respectively given by

$$\omega_{rr} = \frac{a\omega_{\mathrm{A}} + b\omega_{\mathrm{B}}}{a + b}, \tag{13}$$

$$\omega_{\theta\theta} = \frac{a + b}{a/\omega_{\mathrm{A}} + b/\omega_{\mathrm{B}}}, \tag{14}$$

where a, ω_{A} and b, ω_{B} are flare angles, material parameters corresponding to the blue material and the brown material, respectively. For finite-element simulations, we set $a = b = 2°$, $\kappa_{\mathrm{A}} = 3000\,\mathrm{W\,m^{-1}\,K^{-1}}$, $\sigma_{\mathrm{A}} = 10^{-14}\,\mathrm{m^2}$ for the blue material, and $\kappa_{\mathrm{B}} = 0.3\,\mathrm{W\,m^{-1}\,K^{-1}}$, $\sigma_{\mathrm{B}} = 10^{-10}\,\mathrm{m^2}$ for the brown material. κ_{A} and κ_{B} are also the average thermal conductivities of the porous media plus the fluid. The porosity of the two materials are both $\phi = 0.2$. These parameters help to approximately realize $\boldsymbol{\kappa} = \mathrm{diag}\,(1500,\, 0.6)\,\mathrm{W\,m^{-1}\,K^{-1}}$ and $\boldsymbol{\sigma} = \mathrm{diag}\,(50,\, 0.02) \times 10^{-12}\,\mathrm{m^2}$ for the chameleonlike shell shown in Figures 2-4. The structures presented in Figure 6(a)-(c) are applied in Figure 6(a1)-(a8), Figure 6(b1), (b2), and (c1), (c2), respectively. The second, third, and forth rows in Figure 6 correspond to the first rows in Figures 2-4, respectively. The corresponding same temperature distributions and pressure distributions validate the feasibility of the layer structures. Next, we look for practical systems to realize the chameleonlike metashell. We find that carbon nanotube may be a potential candidate. On one hand, the water transport in it has been widely studied [1-8]. On the other hand, carbon nanotube has high thermal conductivity up to $3000\,\mathrm{W\,m^{-1}\,K^{-1}}$. Moreover, aerogel may be another candidate which has low thermal conductivity

about 0.03 W m^{-1} K^{-1}. The permeabilities may be adjusted by filling the carbon nanotube and aerogel.

Nevertheless, we only consider the thermal convection-conduction process in steady states, and the chameleonlike metashell is well-behaved. Certainly, the chameleonlike metashell in transient states can be expected as well, if we take the density and heat capacity into account [41]

$$\rho C\frac{\partial T}{\partial t}+\rho_{\mathrm{f}}C_{\mathrm{f}}\left(\boldsymbol{v}\cdot\boldsymbol{\nabla}T\right)+\boldsymbol{\nabla}\cdot\boldsymbol{j}=0, \tag{15}$$

where ρC is given by $\rho C=(1-\phi)\rho_{\mathrm{s}}C_{\mathrm{s}}+\phi\rho_{\mathrm{f}}C_{\mathrm{f}}$. Here, ρ_{s} and C_{s} denote the density and heat capacity of the porous media, respectively. We take the left two columns in Figure 2 as an example. The results for time $t=0.001$ s and $t=0.002$ s are presented in the left two columns and the right two columns in Figure 7, respectively. The density and heat capacity of the porous media in regions I, II, and III are $\rho_{\mathrm{s}}=5\times10^{2}$ kg m^{-3} and $C_{\mathrm{s}}=5\times10^{2}$ J kg^{-1} K^{-1}. The initial temperature and pressure are 293 K and 0 Pa, respectively. The scalar fields outside the chameleonlike metashell and the comparative shell are approximately the same, which illustrates that the chameleonlike metashell also works in transient regime. It takes about 0.006 s to reach the steady states, and the results are just the left two columns in Figure 2. Compared with the thermal field, the pressure field is established instantaneously because there is almost no difference between the pressure fields at $t=0.001$ s and $t=0.002$ s.

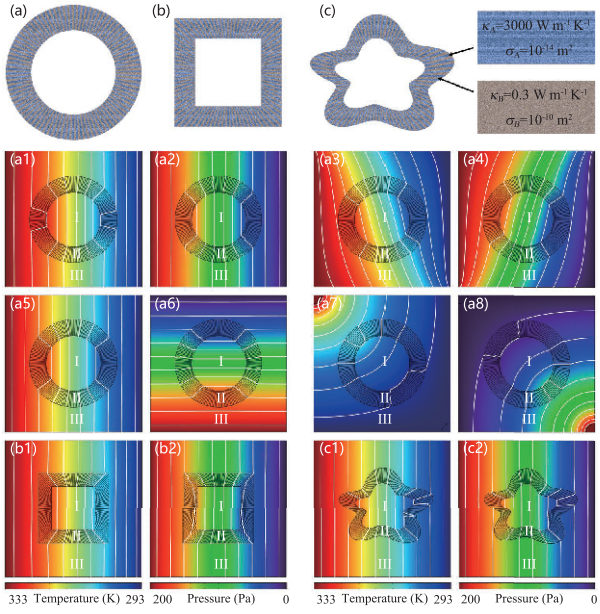

Figure 6 (Color online) Finite-element simulations with isotropic materials and layer structures. The first row exhibits three layer structures with two isotropic materials to realize the parameters for the chameleonlike shell shown in Figures 2-4. Except for the chameleonlike metashell, the other parameters of the second, third, and forth rows are the same as those of the first rows in Figures 2-4.

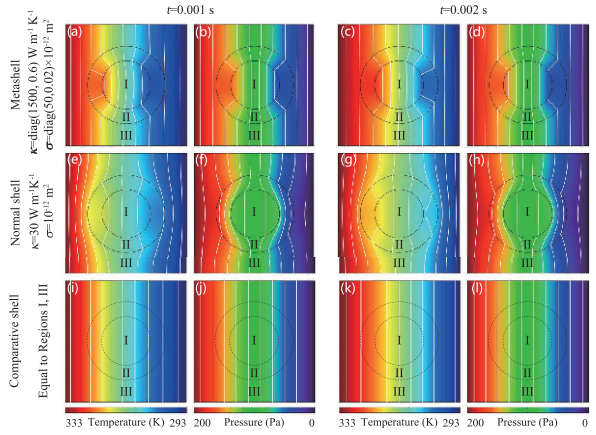

Figure 7 (Color online) Finite-element simulations in transient regime (dominated by eq. (15)). All the parameters are the same as those of the left two columns in Figure 2.

The premises of this work are the validations of eqs. (4) and (5). If the Reynolds number is very large, Darcy's law is no longer solid, and the Brinkman-Stokes flow and turbulent flow should be considered [47-49]. If the phonon effect is taken into consideration [50-53], Fourier's law may be also invalid. Also, radiation is ignored in this work because it is unimportant compared with convection and conduction. However, in some specific cases, radiation may play a key role in heat transfer [54, 55].

In summary, we have proposed the concept of chameleonlike metashells in microfluidics, which is passive, but can exhibit adaptive responses to the inside object. Theoretical analyses and finite-element simulations both validate the proposed scheme. This work can be helpful to explore more intelligent metamaterials in microfluidics, to design all-purpose materials, to camouflage the size of inside objects, and to effectively control thermal convection-conduction processes.

This work was supported by the National Natural Science Foundation of China (Grant No. 11725521).

1 J. C. McDonald, D. C. Duffy, J. R. Anderson, D. T. Chiu, H. Wu, O. J. A. Schueller, and G. M. Whitesides, Electrophoresis **21**, 27 (2000).
2 A. Zahab, L. Spina, P. Poncharal, and C. Marliére, Phys. Rev. B **62**, 10000 (2000).
3 G. Hummer, J. C. Rasaiah, and J. P. Noworyta, Nature **414**, 188 (2001).
4 T. Thorsen, S. J. Maerkl, and S. R. Quake, Science **298**, 580 (2002).
5 A. I. Kolesnikov, J. M. Zanotti, C. K. Loong, P. Thiyagarajan, A. P. Moravsky, R. O. Loutfy, and C. J. Burnham, Phys. Rev. Lett. **93**, 035503 (2004).
6 H. A. Stone, A. D. Stroock, and A. Ajdari, Annu. Rev. Fluid Mech. **36**, 381 (2004).
7 T. M. Squires, and S. R. Quake, Rev. Mod. Phys. **77**, 977 (2005).
8 G. M. Whitesides, Nature **442**, 368 (2006).
9 C. Z. Fan, Y. Gao, and J. P. Huang, Appl. Phys. Lett. **92**, 251907 (2008).
10 S. Narayana, and Y. Sato, Phys. Rev. Lett. **108**, 214303 (2012).

11 R. Schittny, M. Kadic, S. Guenneau, and M. Wegener, Phys. Rev. Lett. **110**, 195901 (2013), arXiv: 1210.2810.
12 X. He, and L. Z. Wu, Sci. China-Phys. Mech. Astron. **56**, 1373 (2013).
13 H. Y. Xu, X. H. Shi, F. Gao, H. D. Sun, and B. L. Zhang, Phys. Rev. Lett. **112**, 054301 (2014).
14 T. C. Han, X. Bai, D. L. Gao, J. T. L. Thong, B. W. Li, and C. W. Qiu, Phys. Rev. Lett. **112**, 054302 (2014).
15 Y. G. Ma, Y. C. Liu, M. Raza, Y. D. Wang, and S. L. He, Phys. Rev. Lett. **113**, 205501 (2014), arXiv: 1405.6949.
16 W. X. Tang, Z. L. Mei, and T. J. Cui, Sci. China-Phys. Mech. Astron. **58**, 127001 (2015).
17 T. C. Han, P. Yang, Y. Li, D. Y. Lei, B. W. Li, K. Hippalgaonkar, and C. W. Qiu, Adv. Mater. **30**, 1804019 (2018).
18 X. He, and L. Z. Wu, Phys. Rev. E **88**, 033201 (2013).
19 L. W. Zeng, and R. X. Song, Appl. Phys. Lett. **104**, 201905 (2014).
20 T. Z. Yang, X. Bai, D. L. Gao, L. Z. Wu, B. W. Li, J. T. L. Thong, and C. W. Qiu, Adv. Mater. **27**, 7752 (2015).
21 L. J. Xu, S. Yang, and J. P. Huang, Phys. Rev. Appl. **11**, 034056 (2019).
22 K. P. Vemuri, and P. R. Bandaru, Appl. Phys. Lett. **104**, 083901 (2014).
23 T. Z. Yang, K. P. Vemuri, and P. R. Bandaru, Appl. Phys. Lett. **105**, 083908 (2014).
24 K. P. Vemuri, F. M. Canbazoglu, and P. R. Bandaru, Appl. Phys. Lett. **105**, 193904 (2014).
25 G. Q. Xu, H. C. Zhang, Y. Jin, S. Li, and Y. Li, Opt. Express **25**, A419 (2017).
26 T. C. Han, X. Bai, J. T. L. Thong, B. W. Li, and C. W. Qiu, Adv. Mater. **26**, 1731 (2014).
27 X. He, and L. Z. Wu, Appl. Phys. Lett. **105**, 221904 (2014).
28 T. Z. Yang, Y. Su, W. Xu, and X. D. Yang, Appl. Phys. Lett. **109**, 121905 (2016).
29 L. J. Xu, C. R. Jiang, J. Shang, R. Z. Wang, and J. P. Huang, Eur. Phys. J. B **90**, 221 (2017).
30 R. Hu, S. L. Zhou, Y. Li, D. Y. Lei, X. B. Luo, and C. W. Qiu, Adv. Mater. **30**, 1707237 (2018).
31 S. L. Zhou, R. Hu, and X. B. Luo, Int. J. Heat Mass Transfer **127**, 607 (2018).
32 L. J. Xu, R. Z. Wang, and J. P. Huang, J. Appl. Phys. **123**, 245111 (2018).
33 L. J. Xu, and J. P. Huang, Phys. Lett. A **382**, 3313 (2018).
34 Y. R. Qu, Q. Li, L. Cai, M. Y. Pan, P. Ghosh, K. K. Du, and M. Qiu, Light Sci. Appl. **7**, 26 (2018).
35 Y. Li, X. Bai, T. Z. Yang, H. Luo, and C. W. Qiu, Nat. Commun. **9**, 273 (2018).
36 L. J. Xu, S. Yang, and J. P. Huang, Phys. Rev. E **98**, 052128 (2018).
37 L. J. Xu, S. Yang, and J. P. Huang, Phys. Rev. E **99**, 022107 (2019).
38 Y. A. Urzhumov, and D. R. Smith, Phys. Rev. Lett. **107**, 074501 (2011), arXiv: 1106.2282.
39 Y. Li, K. J. Zhu, Y. G. Peng, W. Li, T. Yang, H. X. Xu, H. Chen, X. F. Zhu, S. Fan, and C. W. Qiu, Nat. Mater. **18**, 48 (2019).
40 G. L. Dai, J. Shang, and J. P. Huang, Phys. Rev. E **97**, 022129 (2018).
41 G. L. Dai, and J. P. Huang, J. Appl. Phys. **124**, 235103 (2018).
42 L. J. Xu, S. Yang, and J. P. Huang, Phys. Rev. Appl. **11**, 054071 (2019).
43 L. J. Xu, and J. P. Huang, Europhys. Lett. **125**, 64001 (2019).
44 L. J. Xu, and J. P. Huang, Eur. Phys. J. B **92**, 53 (2019).
45 T. C. Han, X. Bai, D. Liu, D. L. Gao, B. W. Li, J. T. L. Thong, and C. W. Qiu, Sci. Rep. **5**, 10242 (2015), arXiv: 1412.0394.
46 T. Y. Chen, C. N. Weng, and Y. L. Tsai, J. Appl. Phys. **117**, 054904 (2015).
47 Y. A. Urzhumov, and D. R. Smith, Phys. Rev. E **86**, 056313 (2012), arXiv: 1212.5201.
48 P. T. Bowen, D. R. Smith, and Y. A. Urzhumov, Phys. Rev. E **92**, 063030 (2015).
49 D. R. Culver, E. Dowell, D. Smith, Y. Urzhumov, and A. Varghese, J. Fluids **2016**, 1 (2016).
50 B. W. Li, L. Wang, and G. Casati, Phys. Rev. Lett. **93**, 184301 (2004).
51 B. W. Li, L. Wang, and G. Casati, Appl. Phys. Lett. **88**, 143501 (2006).
52 L. Wang, and B. W. Li, Phys. Rev. Lett. **99**, 177208 (2007), arXiv: 0709.0032.
53 N. B. Li, J. Ren, L. Wang, G. Zhang, P. Hänggi, and B. W. Li, Rev. Mod. Phys. **84**, 1045 (2012), arXiv: 1108.6120.
54 P. Ben-Abdallah, and S. A. Biehs, Phys. Rev. Lett. **112**, 044301 (2014), arXiv: 1310.0002.
55 V. Kubytskyi, S. A. Biehs, and P. Ben-Abdallah, Phys. Rev. Lett. **113**, 074301 (2014), arXiv: 1404.4793.